

TWO TRANSITING LOW DENSITY SUB-SATURNS FROM K2

ERIK A. PETIGURA^{1,10}, ANDREW W. HOWARD², ERIC D. LOPEZ³, KATHERINE M. DECK^{1,11}, BENJAMIN J. FULTON^{2,12}, IAN J. M. CROSSFIELD^{4,13}, DAVID R. CIARDI⁵, EUGENE CHIANG^{6,7}, EVE J. LEE⁶, HOWARD ISAACSON⁶, CHARLES A. BEICHMAN¹, BRAD M. S. HANSEN⁸, JOSHUA E. SCHLIEDER^{9,14}, EVAN SINUKOFF²

Draft version May 8, 2022

ABSTRACT

We report the discovery and confirmation of two sub-Saturn planets orbiting a bright ($V = 11.3$), metal-rich ($[\text{Fe}/\text{H}] = 0.42 \pm 0.04$ dex) G3 dwarf in the K2 Campaign 2 field. The planets are $5.68 \pm 0.56 R_{\oplus}$ and $7.82 \pm 0.72 R_{\oplus}$ and have orbital periods of 20.8851 ± 0.0003 d and 42.3633 ± 0.0006 d, near to the 2:1 mean-motion resonance. We obtained 32 radial velocities (RVs) with Keck/HIRES and detected the reflex motion due to EPIC-203771098b and c. These planets have masses of $21.0 \pm 5.4 M_{\oplus}$ and $27.0 \pm 6.9 M_{\oplus}$, respectively. With low densities of $0.63 \pm 0.25 \text{ g cm}^{-3}$ and $0.31 \pm 0.12 \text{ g cm}^{-3}$, respectively, the planets require thick envelopes of H/He to explain their large sizes and low masses. Interior structure models predict that the planets have fairly massive cores of $17.6 \pm 4.3 M_{\oplus}$ and $16.1 \pm 4.2 M_{\oplus}$, respectively. They may have formed exterior to their present locations, accreted their H/He envelopes at large orbital distances, and migrated in as a resonant pair. The proximity to resonance, large transit depths, and host star brightness offer rich opportunities for TTV follow-up. Finally, the low surface gravities of the EPIC-203771098 planets make them favorable targets for transmission spectroscopy by *HST*, *Spitzer*, and *JWST*.

1. INTRODUCTION

The prime *Kepler* mission (2009–2013) transformed our understanding of the prevalence and properties of extrasolar planets. In particular, statistical analyses showed that planets the size of Neptune and smaller vastly outnumber larger planets within 1 AU of GK dwarf stars (Howard et al. 2012; Fressin et al. 2013; Petigura et al. 2013). For example, 51% of GK stars host a $R_P = 1\text{--}4 R_{\oplus}$ planet with $P = 5\text{--}100$ d, while only 4.5% of such stars host a $R_P = 4\text{--}16 R_{\oplus}$ planet in the same period range (Petigura et al. 2013).

Kepler detected thousands of Earth-size and Sub-Neptune-size planets and a much smaller number of Jovians ($R_P = 8\text{--}16 R_{\oplus}$) and sub-Saturns ($R_P = 4\text{--}8 R_{\oplus}$) due to their comparative scarcity. Of these, only a small subsample orbit bright stars where follow-up observations such as radial velocity (RV) mass measurements

and transmission spectroscopy are feasible. A major next step in exoplanet science is identifying transiting planets of all sizes orbiting bright stars.

Following the failure of two of the four reaction wheels onboard the *Kepler Space Telescope*, NASA began operating the telescope in a new mode called *K2* (Howell et al. 2014). During *K2* operations, the spacecraft observes a different region of the ecliptic plane every ~ 85 d. By June 2016, *Kepler* will have observed 10 additional fields in the *K2* mode, casting a wider net for planets around bright stars that are sparsely distributed on the sky.

K2 observations will improve our understanding of sub-Saturns. Around GK stars, sub-Saturns are almost twice as common as Jovians: 2.9% of such stars host a sub-Saturn compared to the 1.6% that host a Jovian (Petigura et al. 2013). Despite their relative abundance, few sub-Saturns have reliably measured masses and radii. The Exoplanet Orbit Database (Han et al. 2014)¹⁵ lists 13 sub-Saturns with density measured to 50% or better compared to 174 Jovians. Ground-based transit surveys have a strong bias toward finding Jovian-size planets. In addition, Jovian-size planets have typical masses of $\sim 100\text{--}10,000 M_{\oplus}$ vs. $\sim 10\text{--}100 M_{\oplus}$ for sub-Saturns, making precise RV mass measurements more feasible for Jovians.

Here we present the discovery of two sub-Saturn planets orbiting EPIC-203771098. The planets have radii of $5.68 \pm 0.56 R_{\oplus}$ and $7.82 \pm 0.72 R_{\oplus}$ and orbital periods of 20.8851 ± 0.0003 d and 42.3633 ± 0.0006 d, near the 2:1 mean-motion resonance. Their host star is a bright ($V = 11.3$) G3 dwarf which allowed us to obtain precise RV mass constraints using Keck/HIRES. The planets have masses of $21.0 \pm 5.4 M_{\oplus}$ and $27.0 \pm 6.9 M_{\oplus}$, respectively. We describe our photometric, imaging, and spectroscopic observations in Section 2. In Section 3, we explain how we extract stellar and planet properties

¹ California Institute of Technology, Pasadena, California, U.S.A. petigura@caltech.edu

² Institute for Astronomy, University of Hawaii, 2680 Woodlawn Drive, Honolulu, HI, USA

³ Institute for Astronomy, University of Edinburgh, Blackford Hill, Edinburgh, EH9 3HJ

⁴ Lunar & Planetary Laboratory, University of Arizona, 1629 E. University Blvd., Tucson, AZ, USA

⁵ NASA Exoplanet Science Institute, California Institute of Technology, 770 S. Wilson Ave., Pasadena, CA, USA

⁶ Astronomy Department, University of California, Berkeley, CA, USA

⁷ Department of Earth and Planetary Science, University of California Berkeley, Berkeley, CA 94720-4767, USA

⁸ Department of Physics & Astronomy and Institute of Geophysics & Planetary Physics, University of California Los Angeles, Los Angeles, CA 90095

⁹ NASA Ames Research Center, Moffett Field, CA, USA

¹⁰ Hubble Fellow

¹¹ California Institute of Technology, Joint Center for Planetary Astronomy Fellow

¹² NSF Graduate Research Fellow

¹³ NASA Sagan Fellow

¹⁴ NASA Postdoctoral Program Fellow

from our observations. In Section 4, we discuss the likely distribution in mass between core and envelope and how that relates to the planets’ formation histories. We also investigate system dynamics in the context of long-term stability. We also place EPIC-203771098b and c in the context of other sub-Saturns and discuss future follow-up opportunities. We give a brief summary in Section 5.

2. OBSERVATIONS

2.1. Discovery in *K2* Photometry

EPIC-203771098 was observed during *K2* Campaign 2 with nearly continuous photometry from 2014 Aug 23 to 2014 Nov 13. The star is listed as EPIC-203771098 in the Mikulski Archive for Space Telescopes (MAST). It was selected for *K2* observations based on *K2* Guest Observer proposal GO2104 (PI: Petigura). We list the star’s identifying information, coordinates, and photometric properties in Table 1.

We extracted the photometry of EPIC-203771098 from the *Kepler* pixel data, which we downloaded from the MAST. Our photometric extraction pipeline is described in Crossfield et al. (2015) and Petigura et al. (2015). In brief, during *K2* operations the telescope is torqued by solar radiation pressure, causing it to roll around the boresight. This motion causes stars to drift across the CCD by ~ 1 pixel every ~ 6 hours. As stars sample different pixel-phases, inter-pixel sensitivity variations cause the apparent brightness of the star to change. We solve for the roll angle between each frame and an arbitrary reference frame. We model the time- and roll-dependent brightness variations using a Gaussian process. We also adjust the size of our circular extraction aperture to minimize the residual noise in the corrected light curve. This balances two competing effects: larger apertures yield smaller systematic errors while smaller apertures incur less background noise. The circular extraction aperture ($r = 3$ pixel) is shown in Figure 1. Figure 2 shows both the raw and corrected photometry for EPIC-203771098. Our calibrated photometry is available as an online supplement.

We searched through the calibrated photometry using the TERRA algorithm (Petigura et al. 2013). While two sets of transits are clearly visible by eye in the detrended *K2* photometry for this star, we rely on TERRA to search through the photometry of 10,000–20,000 light curves per *K2* Campaign. After identifying the transits of planets b and c, we re-ran TERRA on the photometry of EPIC-203771098 with the in-transit points removed and did not identify any additional transit candidates.

2.2. Imaging

2.3. Archival and Adaptive Optics Imaging

We obtained near-infrared adaptive optics images of EPIC-203771098 using NIRC2 on the 10 m Keck II Telescope on the night of 2015-04-01 UT. We used the 1024×1024 NIRC2 array and the natural guide star system; the target star was bright enough to be used as the guide star. The data were acquired using the narrow-band Br- γ filter using the narrow camera field of view with a pixel scale of 9.942 mas/pixel. The Br- γ filter has a narrower passband (2.13–2.18 μm), but a similar central wavelength (2.15 μm) compared the Ks filter (1.95–

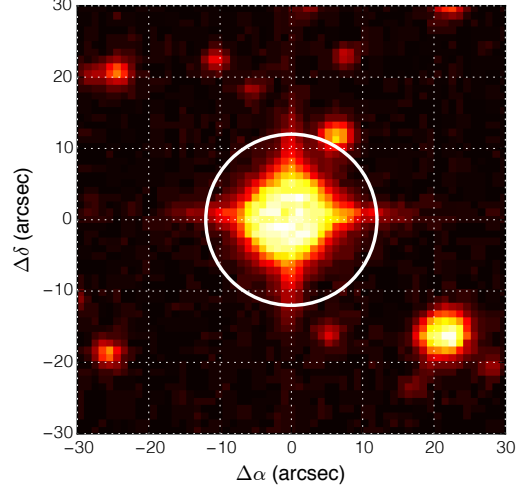


FIG. 1.— POSS2 red planets observed in 1991. EPIC-203771098 is in the center of the frame. The white circle shows the extent of the circular aperture used to extract the photometry of EPIC-203771098. No stars fall within our aperture that could dilute the light of EPIC-203771098. EPIC-203772026 sits just outside the border of our aperture. However, with $\Delta K_p = 4.9$ (EPIC catalog), it has negligible effect on the transit radius.

2.34 μm ; 2.15 μm) and allows for longer integration times before saturation. A 3-point dither pattern was utilized to avoid the noisier lower left quadrant of the NIRC2 array. The 3-point dither pattern was observed three times with 1 co-add and a 5.5 second integration time for a total on-source exposure time of $3 \times 3 \times 5.5$ s = 49.5 s.

The target star was measured with a resolution of 0.055 arcsec (FWHM). No other stars were detected within the 10 arcsec field of view of the camera. In the Br- γ filter, the data are sensitive to stars that have K -band contrast of $\Delta K = 4.2$ at a separation of 0.1 arcsec and $\Delta K = 7.9$ at 0.5 arcsec from the central star. We estimate the sensitivities by injecting fake sources with a signal-to-noise ratio of 5 into the final combined images at distances of $N \times \text{FWHM}$ from the central source, where N is an integer. Our combined NIRC2 image and contrast curve are shown in Figure 4.

2.4. Spectroscopy

We observed EPIC-203771098 with the High Resolution Echelle Spectrometer (HIRES; Vogt et al. 1994) on the 10 m Keck Telescope I. Between 24 June and 3 October 2015, we obtained 32 spectra through an iodine cell mounted directly in front of the spectrometer slit. The iodine cell imprints a dense forest of absorption lines which serve as a wavelength reference. We also obtained a “template” spectrum without iodine. We used an exposure meter to achieve a constant signal to noise ratio of 110 per HIRES pixel on blaze near 550 nm. Exposure times were in the range 6–12 min. RVs were determined using standard procedures of the California Planet Search (CPS; Howard et al. 2010) including forward modeling of the stellar and iodine spectra convolved with the instrumental response (Marcy & Butler 1992; Valenti et al. 1995). The radial velocities are tabulated in Table 3. We also list the measurement uncertainty of each RV point, which range from 1.5 to 2.0 m s^{-1} from the uncertainty on the mean RV of the ~ 700 spectral chunks

TABLE 1
STELLAR PARAMETERS OF $K2 - XX$

Parameter	Units	Value	Source
Identifying Information			
EPIC ID	—	203771098	EPIC
2MASS ID	—	16101770-2459251	2MASS
α R.A.	h:m:s	16:10:17.69	EPIC
δ Dec.	d:m:s	-24:59:25.19	EPIC
Photometric Properties			
K_p	mag	11.65	EPIC
B	mag	12.22 ± 0.20	APASS
V	mag	11.28 ± 0.10	APASS
g'	mag	13.99 ± 0.90	APASS
r'	mag	10.71 ± 0.22	APASS
i'	mag	10.64 ± 0.01	APASS
J	mag	9.63 ± 0.02	2MASS
H	mag	9.29 ± 0.02	2MASS
K_s	mag	9.18 ± 0.02	2MASS
Spectroscopic Properties			
T_{eff}	K	5743 ± 60	SM, this paper
$\log g$	dex	4.29 ± 0.07	SM, this paper
[Fe/H]	dex	0.42 ± 0.04	SM, this paper
$v \sin i$	km s^{-1}	< 2	SM, this paper
S_{HK}	—	0.128	this paper
$\log R'_{\text{HK}}$	dex	-5.258	this paper
Derived Properties			
μ_{α}	mas yr^{-1}	-60.6 ± 2.5	Zacharias et al. (2012)
μ_{δ}	mas yr^{-1}	-65.4 ± 2.4	Zacharias et al. (2012)
M_{\star}	M_{\odot}	1.12 ± 0.05	SM, iso, this paper
R_{\star}	R_{\odot}	1.21 ± 0.11	SM, iso, this paper
ρ_{\star}	g cm^{-3}	0.89 ± 0.23	SM, iso, this paper
L_{\star}	L_{\odot}	1.44 ± 0.33	SM, iso, this paper
Distance	pc	181 ± 17	SM, iso, this paper
Age	Gyr	3.2–6.9	SM, iso, this paper

NOTE. — SM: SpecMatch spectrum synthesis code (Petigura 2015). iso: isochrones interface to the Dartmouth suite of stellar isochrones (Morton 2015; Dotter et al. 2008).

used in the RV pipeline.

We measured the strength of the Ca II H & K lines and found that EPIC-203771098 is an inactive star. We see no emission reversal in the cores of these lines. Table 1 lists the median values of S_{HK} using the method of Isaacson & Fischer (2010) and $\log R'_{\text{HK}}$ computed using $B - V = 0.673$ estimated from T_{eff} according to the relation from Valenti & Fischer (2005).

We searched for companions with separations smaller than ≈ 0.1 arcsec, where our sensitivity to sources from AO imaging declines (see Figure 4). Adopting the methodology in Kolbl et al. (2015), we searched for spectroscopic binaries in our HIRES spectrum. We detect no secondary set of lines from a star having $\Delta V < 5$ mag shifted by more than 15 km/s relative to the lines of the primary star. Shifts of $\Delta v \gtrsim 15$ km/s correspond to orbital separations of $\lesssim 4$ AU.

3. ANALYSIS

3.1. Stellar Properties

We analyzed our iodine-free template spectrum from HIRES using the SpecMatch spectrum synthesis code (Petigura 2015). SpecMatch is a general tool for extracting stellar T_{eff} , $\log g$, [Fe/H], and $v \sin i$ by fitting high-resolution spectra. SpecMatch generates syn-

thetic spectra at arbitrary T_{eff} , $\log g$, [Fe/H], and $v \sin i$ by interpolating between LTE models of Coelho et al. (2005) and applying broadening kernels that account for line broadening due to stellar rotation and macroturbulence and the instrumental profile of the spectrometer. T_{eff} , $\log g$, [Fe/H], and $v \sin i$ are adjusted in order to yield the best-matching spectrum in χ^2 sense. We determined that EPIC-203771098 is a metal-rich G3 star having $T_{\text{eff}} = 5743 \pm 60$ K, $\log g = 4.29 \pm 0.07$ dex, [Fe/H] = 0.42 ± 0.04 dex, and $v \sin i < 2 \text{ m s}^{-1}$. Our uncertainties in T_{eff} and [Fe/H] are based on comparisons with touchstone stars in the literature with stellar parameters from asteroseismology (Huber et al. 2013), LTE-modelling (Valenti & Fischer 2005; Torres et al. 2012), and Rossiter-McLaughlin measurements (Albrecht et al. 2012).

We converted spectroscopic parameters into physical stellar properties using the isochrones python package (Morton 2015), which provides a convenient interface to the Dartmouth suite of stellar isochrones (Dotter et al. 2008). EPIC-203771098 is slightly larger and more massive than the Sun: $M_{\star} = 1.12 \pm 0.05 M_{\odot}$ and $R_{\star} = 1.21 \pm 0.11 R_{\odot}$. We list the spectroscopic and derived physical properties of EPIC-203771098 in Table 1.

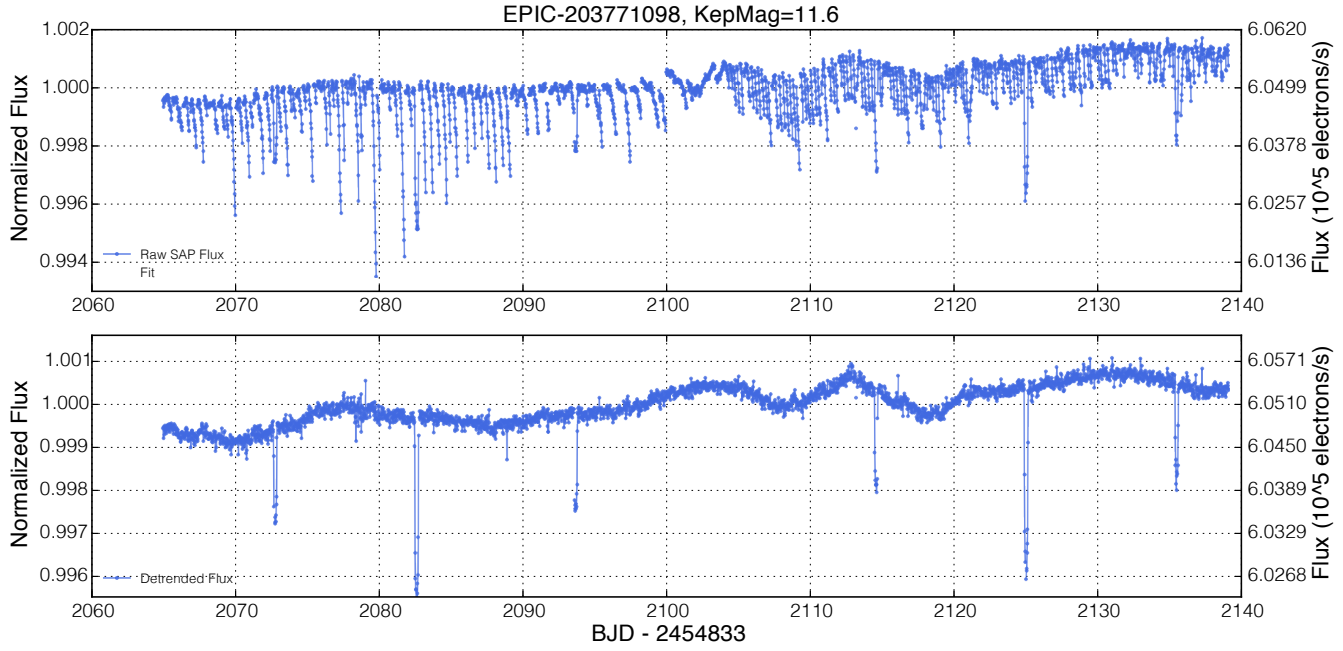


FIG. 2.— *Top:* Raw photometry computed by summing the background-subtracted counts inside a circular aperture (3 pixel radius) centered on EPIC-203771098. *Bottom:* Photometry after correcting for variations due to telescope roll angle. Noise on three-hour timescales has been reduced by a factor of 8. The $\sim 0.1\%$ variability gives an upper limit to intrinsic stellar variability. However, since stars drift perpendicular to the roll direction over the course of a campaign, it is difficult to disentangle long-term astrophysical variability from position-dependent variability. The data used to produce the bottom panel is included as an electronic supplement.

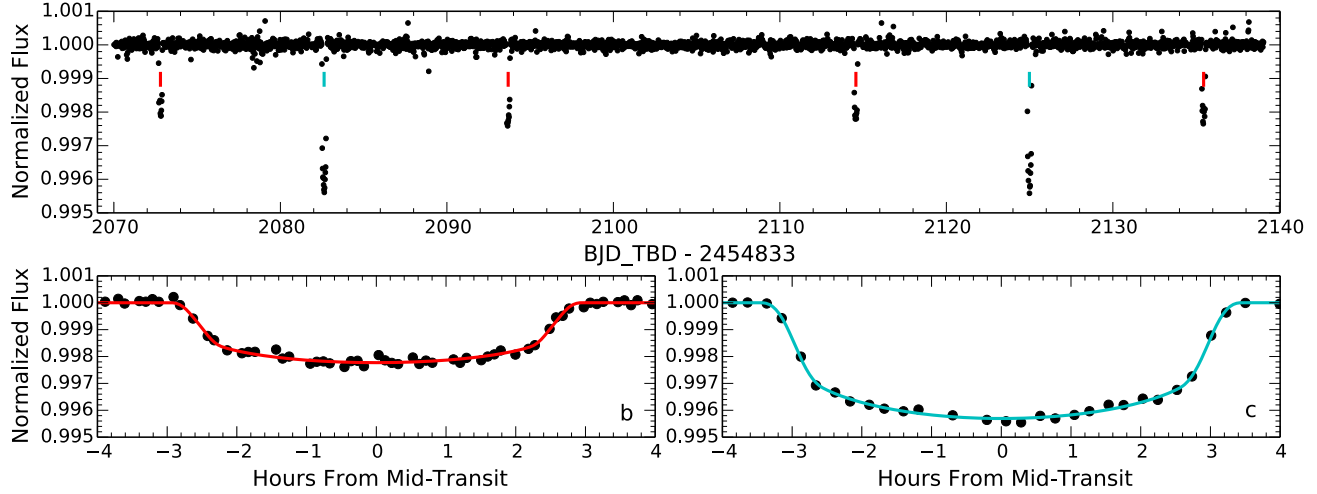


FIG. 3.— *Top:* Calibrated *K2* photometry for EPIC-203771098. Vertical ticks indicate the times of transit. *Bottom:* Phase-folded photometry and best fit light curves for each planet. Best fit parameters from light curve fitting are tabulated in Table 2.

3.2. Light curve modeling

We analyzed *K2* transit light curve using the same approach described by Crossfield et al. (2015). In brief, we fit each planet’s transit separately using a minimization and Markov Chain Monte Carlo (MCMC) analysis (Foreman-Mackey et al. 2013a) using the `batman` code (Kreidberg 2015) to model the light curves that assumes a linear transit ephemeris for each planet.

When modeling the transit photometry, we adopt a quadratic limb-darkening law. We used the `LDTk` Limb Darkening Toolkit (Parviainen & Aigrain 2015) to derive limb-darkening coefficients of $u_1 = 0.568 \pm 0.003$

$u_2 = 0.098 \pm 0.005$. We doubled the uncertainties associated with the limb-darkening parameters and incorporated them as Gaussian priors in the MCMC light curve analysis. All of the MCMC parameters show unimodal distributions. The transit profiles alone do little to constrain orbital eccentricity and give upper limits on $e_b < 0.78$ and $e_c < 0.81$ at 95% confidence. Figure 3 shows the EPIC-203771098 photometry and best fit models, and Table 2 summarizes the final values and uncertainties.

The transit profile constrains the mean stellar density if one assumes a circular orbit. Since we fit each

TABLE 2
PLANET PARAMETERS

Parameter	Units	b	c
Light curve fitting			
T_0	BJD _{TDB} − 2454833	2072.7948 ± 0.0007	2082.6251 ± 0.0004
P	d	20.8851 ± 0.0003	42.3633 ± 0.0006
i	deg	89.25 ^{+0.49} _{−0.61}	89.76 ^{+0.18} _{−0.21}
R_P/R_*	%	4.31 ^{+0.17} _{−0.08}	5.94 ^{+0.10} _{−0.04}
T_{14}	hr	5.48 ^{+0.07} _{−0.04}	6.47 ^{+0.04} _{−0.03}
T_{23}	hr	4.95 ^{+0.05} _{−0.11}	5.70 ^{+0.03} _{−0.06}
R_*/a	—	0.035 ^{+0.005} _{−0.002}	0.019 ^{+0.001} _{−0.000}
b	—	0.37 ^{+0.22} _{−0.24}	0.22 ^{+0.17} _{−0.16}
$\rho_{\star,\text{circ}}$	g cm ^{−3}	1.00 ^{+0.21} _{−0.33}	1.47 ^{+0.31} _{−0.23}
a	AU	0.154 ± 0.002	0.247 ± 0.004
S_{inc}	S_{\oplus}	60 ± 14	24 ± 5
T_{eq}	K	767 ± 177	606 ± 139
R_P	R_{\oplus}	5.68 ± 0.56	7.82 ± 0.72
Circular RV model (adopted)			
K	m s ^{−1}	4.5 ± 1.1	4.6 ± 1.2
γ	m s ^{−1}	−2.5 ± 0.9	
dv/dt	m s ^{−1} yr ^{−1}	−23.9 ± 9.7	
σ_{jit}	m s ^{−1}	3.4 ± 0.7	
M_P	M_{\oplus}	21.0 ± 5.4	27.0 ± 6.9
ρ	g cm ^{−3}	0.63 ± 0.25	0.31 ± 0.12
Eccentric RV model			
K	m s ^{−1}	5.1 ± 1.2	5.3 ± 1.1
$e \cos \omega_{\star}$	—	0.20 ± 0.09	0.00 ± 0.09
$e \sin \omega_{\star}$	—	−0.06 ± 0.16	−0.02 ± 0.15
e	—	0.24 ^{+0.11} _{−0.11}	< 0.39 (95%)
γ	m s ^{−1}	−2.7 ± 1.0	
dv/dt	m s ^{−1} yr ^{−1}	−22.5 ± 9.2	
σ_{jit}	m s ^{−1}	2.9 ± 0.6	
M_P	M_{\oplus}	23.2 ± 5.3	31.0 ± 6.4
ρ	g cm ^{−3}	0.70 ± 0.26	0.36 ± 0.12

planet separately, we obtain two independent measurements for $\rho_{\star,\text{circ}}$, $1.00^{+0.21}_{−0.33}$ g cm^{−3} and $1.47^{+0.31}_{−0.23}$ g cm^{−3}. In addition we also have a spectroscopic estimate of $\rho_{\star} = 0.89 \pm 0.23$ g cm^{−3}. All three estimates of mean stellar density are consistent at the 2- σ level. In our analysis, we have modeled the light curve as a single unblended star. While our AO and spectroscopic observations rule out stars with $\Delta Kp \lesssim 5$ inside ~ 4 AU and outside ~ 20 AU, we have not covered parameter space entirely. There is a small possibility that our transit profiles could be diluted by an additional star, affecting primarily the derived planet radii. However, we confirm these planets without the need for statistical validation with RVs as described in the following section.

3.3. Radial Velocities

We detected RV variability matching the orbital periods and phases of EPIC-203771098b and c that were measured from the *K2* light curve. Measuring the masses

of these planets (as described below) confirms their existence and rules out false positive scenarios.

We modeled the stellar RV time series as the sum of two Keplerian orbits. We considered both eccentric and circular orbits. Circular orbits require three parameters per planet: orbital period P , time of transit T_0 , and the Doppler semi-amplitude K . In addition, we allowed for an arbitrary RV offset, γ , and a linear acceleration, dv/dt . To assess the quality of a given model we evaluated the log-likelihood, $\ln \mathcal{L}$, according to the prescription given in Howard et al. (2014). This likelihood definition incorporates RV “jitter” (σ_{jit}), an additional RV uncertainty due to astrophysical and instrumental sources. To guard against non-physical values of K and σ_{jit} , we parametrized the model using $\log K$ and $\log \sigma_{\text{jit}}$. We imposed no prior on $\log \sigma_{\text{jit}}$. Because P and T_0 are measured with exquisite precision from the *K2* photometry, we held these parameters fixed during our RV analysis. While the EPIC-203771098bc pair’s proximity to reso-

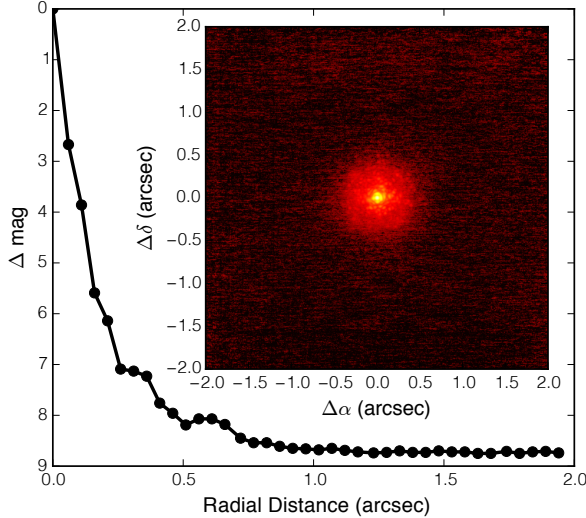


FIG. 4.— NIRC2 K-band image and contrast curve. Our NIRC2 observations using the Br- γ filter rule out companions having K -band contrasts of < 7.9 mag for separations of 0.7–8.0 arcsec. The inset shows a 4×4 arcsec subregion in order to highlight the sensitivity of NIRC2 to companions at small orbital separations.

nance will result in strong dynamical interactions, we expect TTVs on the order of ~ 3 –6 hr, not an appreciable fraction of an orbital period (see Section 4.5.1). Therefore, we do not consider departures from strict Keplerian motion when modeling the RVs.

The red curve in Figure 5 shows the maximum likelihood model which we found using the Limited-Memory Broyden-Fletcher-Goldfarb-Shanno optimization routine (Byrd et al. 1995) as implemented in the `scipy` Python package (Jones et al. 2001). The bottom panels show the maximum likelihood models for each planet individually. We explored the likelihood surface using MCMC as implemented in the `emcee` Python package (Foreman-Mackey et al. 2013b). Table 2 summarizes the median posterior values and the 14% and 86% quantiles. We detected the reflex velocities due to both planets. Assuming circular orbits, EPIC-203771098b and EPIC-203771098c have masses of $21.0 \pm 5.4 M_{\oplus}$ and $27.0 \pm 6.9 M_{\oplus}$, respectively.

Eccentric models included two additional parameters per planet: e , eccentricity and ω_* , the longitude of periastron of the star’s orbit. Following Eastman et al. (2013), we re-parametrized e and ω_* as $\sqrt{e} \cos \omega_*$ and $\sqrt{e} \sin \omega_*$, which mitigates the Lucy-Sweeney bias toward non-zero eccentricity (Lucy & Sweeney 1971). The maximum likelihood model is shown as a blue dashed curve in Figure 5, and the MCMC posteriors are summarized in Table 2. When we included eccentricity in the models, the planets have masses $23.2 \pm 5.3 M_{\oplus}$ and $31.0 \pm 6.4 M_{\oplus}$, respectively. Interestingly, our eccentric models predict $e_b = 0.24^{+0.11}_{-0.11}$ while e_c is consistent with zero (< 0.39 at 95% confidence).

We assessed the relative merits of the eccentric and circular models using the Bayesian Information Criterion (BIC). The BIC is defined as $\text{BIC} = -2 \ln \mathcal{L}_{\max} + k \ln N$ where \mathcal{L}_{\max} is the maximized likelihood, k is the number of free parameters, and N is the number of observations (Schwarz 1978; Liddle 2004). For our RV time series $N = 32$. When comparing two models, the

TABLE 3
RELATIVE RADIAL VELOCITIES

BJD - 2454833	Radial Velocity m s^{-1}	Uncertainty m s^{-1}
2364.81958	6.96	1.59
2364.82510	5.02	1.60
2364.83070	13.81	1.66
2366.82758	1.15	1.65
2367.85265	9.39	1.64
2373.88815	-2.82	1.72
2374.85241	-0.77	1.91
2376.86382	-2.22	1.71
2377.86607	0.15	1.84
2378.83401	2.74	1.65
2380.93080	7.57	1.86
2382.88614	5.14	1.68
2383.82353	0.37	1.90
2384.79994	-1.48	1.69
2384.82899	-2.74	1.68
2384.83972	-5.68	1.72
2388.95596	-3.91	1.71
2395.85726	-5.64	1.64
2402.89876	3.64	1.76
2403.77132	3.54	1.65
2411.75570	-3.75	1.46
2412.79420	-0.11	1.78
2420.80302	0.11	1.64
2421.82280	-2.59	1.76
2422.74212	3.02	1.66
2429.76175	-13.03	1.98
2429.81023	-11.00	1.88
2432.73232	-12.06	1.70
2432.80724	-14.87	1.91
2457.71690	-1.31	1.93
2457.75480	-5.32	1.94
2465.71074	4.87	1.62

model with the lower BIC is preferred. The BIC penalizes models with low likelihood and high complexity. $\text{BIC}(\text{circular}) - \text{BIC}(\text{eccentric}) = -4.9$. Because the best fit circular model has lower BIC, we adopt its associated best fit parameters as our preferred system parameters. However, we discuss the dynamical implications of eccentric orbits in Section 4.3.

We also observe a linear trend in the radial velocities of $-23.9 \pm 9.7 \text{ m s}^{-1} \text{ yr}^{-1}$. This trend is marginally significant and could indicate an additional body in the system. Following Winn et al. (2010), we consider the range of possible $M_P \sin i$ and a that could produce the observed trend. A body on a circular orbit with $M_P \ll M_*$ induces a reflex acceleration of $dv/dt = GM_P/a^2$. The mass and separation of the planet (or star) is given by

$$M_P \sin i \sim 42 M_{\oplus} \left(\frac{a}{1 \text{ AU}} \right)^2.$$

We advocate for future observations of EPIC-203771098 to build a more complete picture of this planetary system.

4. DISCUSSION

4.1. Core-Envelope Structure

EPIC-203771098b & c are among only a handful of transiting sub-Saturns with well-measured masses. With two sub-Saturns in the same system, we have a rare chance to compare the possible compositions of these planets to each other and to the general population of sub-Saturns. We examine possible compositions with the interior and thermal evolution models of Lopez & Fort-

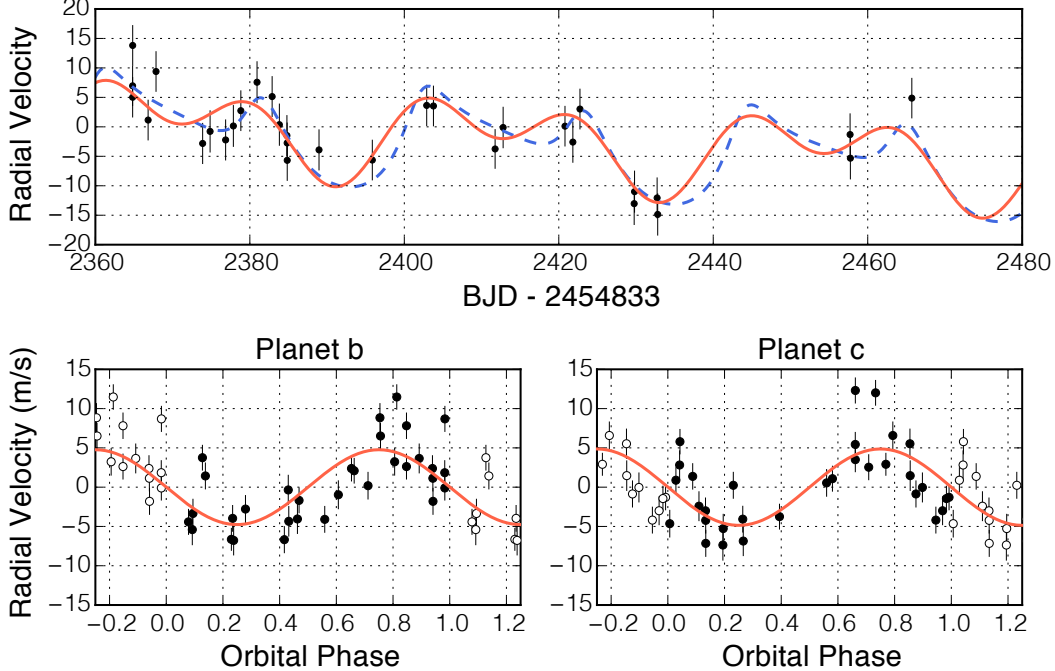


FIG. 5.— The top panel shows the radial velocity time series collected using Keck/HIRES between 24 June 2015 and 03 October 2015. The red line shows the best fit Keplerian, assuming a circular orbit. The blue dashed line shows the best fit Keplerian allowing for eccentricity to vary. While the eccentric solution has higher likelihood than the circular solution $\ln \mathcal{L} = -85.3$ vs -80.1 , it comes at the expense of more free parameters. We adopt the circular solution as our system parameters. The bottom plots show the RVs folded on the ephemerides of planet b and c. In these plots, the contribution of the other planet as well as the contribution from the trend (parametrized by γ and dv/dt) has been removed.

ney (2014) which track the cooling and contraction of planets with H/He envelopes and allow us to convert measured masses, radii, and incident fluxes of EPIC-203771098b & c into estimates of H/He mass fraction.

We modeled planets with solar metallicity H/He envelopes atop a fully differentiated Earth composition core. According to these models, we find that EPIC-203771098b is $24 \pm 8\%$ H/He by mass, while EPIC-203771098c is $48 \pm 9\%$ H/He by mass. EPIC-203771098b & c then have core masses of $17.6 \pm 4.3 M_{\oplus}$ and $16.1 \pm 4.2 M_{\oplus}$, respectively. The uncertainty on the envelope fraction includes the observational uncertainties on planet mass, radius, age, and incident flux along with theoretical uncertainties such as the iron fraction and heat capacity of the rocky core. Our uncertainty in envelope mass is dominated by planet radius errors; our uncertainty in planet core mass is dominated by uncertainties in planet mass.

These planets are sufficiently large that our conclusions are insensitive to variations in the core composition. While pure water cores are likely unphysical, we repeated the above calculations for planets with 98% water cores in order to set a lower bound on the H/He envelope fraction. Using these models of EPIC-203771098b & c, we found envelope mass fractions of $14 \pm 5\%$ & $36 \pm 8\%$ and core masses of $18.0 \pm 4.9 M_{\oplus}$ and $17.2 \pm 5.0 M_{\oplus}$, respectively. The effect of changing the assumed core composition from Earth-like to pure water has a small effect on the derived core masses (within the statistical uncertainties). We adopt $17.6 \pm 4.3 M_{\oplus}$ and $16.1 \pm 4.2 M_{\oplus}$ as the core masses of EPIC-203771098b & c, respectively.

4.2. Formation Scenarios

The inferred core-envelope structures of EPIC-203771098b & c pose some challenges to explaining their formation. How did EPIC-203771098c end up with twice as much gas as EPIC-203771098b despite forming in the same disk with a similar core mass? Another challenge is explaining how EPIC-203771098c is composed of half H/He gas, but somehow avoided runaway accretion as predicted in standard models of core accretion (e.g., Pollack et al. 1996; Lee et al. 2014).

While the different densities of planet pairs like Kepler-36b & c can be understood in terms of differing XUV-driven mass loss histories (Lopez & Fortney 2013), mass loss likely played only a minor role for EPIC-203771098b & c. The planets are only modestly irradiated, and their cores are relatively massive compared to typical hot sub-Neptunes. Using the coupled thermal evolution and photo-evaporation model of Lopez & Fortney (2013), we find that both planets would have only been $\approx 1\%$ more massive at an age of 10 Myr.

The fact that the EPIC-203771098bc pair are near the 2:1 mean-motion resonance suggests they formed at larger orbital separations and experienced convergent inward migration (e.g., Murray & Dermott 2000; see also Deck & Batygin 2015). Formation at $\gtrsim 1$ AU as opposed to their current locations (~ 0.2 AU), together with inward migration, could explain the large inferred envelope fractions (Lee & Chiang 2015a). Lee & Chiang (2015b) derived analytic scaling relations for atmospheric accretion. For planets at $\gtrsim 1$ AU with dust-free atmospheres, they found that the gas-to-core mass ratio scales as $M_{\text{core}}^1 T_{\text{eq}}^{-1.5}$ (equation 24 of their paper), with T_{eq}

equal to the equilibrium surface temperature. The dependence on T_{eq} arises because colder planets have lower opacities and therefore cool and accrete faster. Since EPIC-203771098c presumably formed exterior to EPIC-203771098b and had a lower T_{eq} , these dust-free accretion models may explain, in a natural way, why the outer planet in the EPIC-203771098bc pair has a more massive envelope.

In the case of dusty atmospheres, Lee & Chiang (2015b) found that the accreted gas fraction is independent of local disk temperature. Thus if the early atmospheres of EPIC-203771098b & c were dusty, different formation locations could not alone explain their different envelope masses. Dusty envelopes might still be accommodated if EPIC-203771098b initially formed with a more massive envelope but lost a large fraction of it to a giant impact. Recent studies of giant impacts have found that a collision with an equal mass impactor can reduce a planet's gas fraction by a factor of ~ 2 (Liu et al. 2015; Inamdar & Schlichting 2015), thus providing an alternative explanation for the difference between the inferred gas fractions of EPIC-203771098b and c.

With this one system, it is not possible to distinguish between the formation hypotheses of dust-free gas accretion vs. giant impacts. However, it is intriguing that the longer period planet has the much larger envelope fraction, as we might expect from dust-free gas accretion and convergent migration (Lee & Chiang 2015a). As more sub-Saturns are found and characterized, ensemble properties should shed light on their formation. If stochastic processes like giant impacts determine envelope masses, we expect no correlation between orbital distance and envelope fraction. However, if gas accretion is governed by local disk properties, we should see correlations with orbital distance—as is arguably already observed by the well-known increase in the occurrence rate of Jupiter-mass gas giants beyond ~ 1 AU (Cumming et al. 2008).

Explaining how EPIC-203771098c roughly doubled in mass while accreting gas, yet somehow avoided runaway accretion is difficult in the context of standard models of core accretion (e.g., Pollack et al. 1996; Lee et al. 2014). The Lee & Chiang (2015a) scenario of dust-free gas accretion in a disk coupled with inward migration raises a concern of fine tuning since it requires that EPIC-203771098c reach the threshold of runaway (its gas-to-core ratio is modeled to be $48 \pm 9\%$) without actually running away. However, we note that sub-Saturn-sized planets are not common outcomes of planet formation (2.9% of GK stars host a sub-Saturn with $P < 100$ d; Petigura et al. 2013) and near-resonant sub-Saturns are rarer still.

4.3. System Dynamics

Given the current dataset, we are hesitant to claim a non-zero eccentricity for planet b. However, our eccentric model does have some precedent among previously discovered systems. GJ876c and b have orbital periods of 30.08 d and 61.12 d respectively, and, like EPIC-203771098b and c, lie just outside 2:1 mean-motion resonance (Marcy et al. 1998; Delfosse et al. 1998; Marcy et al. 2001). N-body fits to the GJ876 RVs show that planet c is moderately eccentric ($e = 0.25591 \pm 0.00093$) while planet b has a nearly circular orbit ($e = 0.0292 \pm$

0.0015; Rivera et al. 2010). The high precision eccentricity measurements in this case are from the large Doppler amplitudes (~ 100 m s $^{-1}$) and the detection of resonant interactions.

We consider here the dynamical implications of eccentric orbits, assuming the system has a long-lived orbital architecture. The system dynamics are governed by the two planets' masses, eccentricities, and longitudes of pericenter, ϖ .¹⁶ Instead of performing a uniform exploration of this six-dimensional parameter space, we consider systems drawn from our MCMC exploration of eccentric RV solutions. First, roughly 25% of the models in our MCMC chain satisfy $a_c(1 - e_c) < a_b(1 + e_b)$. Given that the distribution of planet ϖ is nearly uniform, many of these solutions correspond to crossing orbits.

We also considered whether the systems are Hill stable, using the full criterion, which is based on conservation of the quantity $L^2 E$, where L and E are the total orbital angular momentum and energy of the system (Marchal & Bozis 1982; Milani & Nobili 1983). Roughly half of the MCMC realizations fail the Hill criterion. These include all solutions with $e_b \gtrsim 0.3$ or $e_c \gtrsim 0.3$. While eccentricity of planet b ($e_b = 0.24^{+0.11}_{-0.11}$) is likely less than 0.3, the 1- σ confidence interval extends past 0.3. In this case, the system must be in some type of resonant phase protection which prevents close approaches in order to be long-lived (e.g., Gladman 1993; Barnes & Greenberg 2007). On the other hand, orbits which satisfy the Hill criterion, though protected from collisions, are not necessarily long-lived as weak encounters can still lead to large and erratic variations in the orbital elements. To test this, we selected 100 planet masses, orbital eccentricities and longitudes of pericenter randomly from the MCMC chain. We integrated these initial conditions using a Wisdom-Holman mapping with a symplectic corrector employed (Wisdom & Holman 1991; Wisdom et al. 1996). Our timestep was 0.25 days, and we ensured that the fractional energy conservation was high (typically $\sim 10^{-10}$). The integrations lasted for 10^6 years, or ≈ 20 million orbits of the inner planet.

Although roughly half of the orbits failed the Hill criterion, only 9 showed instability during the integrations (deviations in semimajor axes larger than 5% of the initial values). To understand why, we selected the orbits which failed the Hill criterion yet remained long-lived, and looked at the orbital evolution of the eccentricities and the angle $\Delta\varpi = \varpi_b - \varpi_c$ on timescales of 3×10^4 orbits of the inner planet. Roughly 70% show apparently regular evolution, and the majority exhibit libration of $\Delta\varpi$, about zero or π , indicating a resonant protection mechanism. Although there is no preferred value of $\Delta\varpi$ based on the RV data, at high eccentricities the 2:1 resonance is wide, and so it is not surprising that many are in resonance, albeit with large libration amplitudes.

The majority of the remaining 30% of the orbits appear chaotic, with erratic variation of eccentricities and alternations between circulating and libration of $\Delta\varpi$ and/or the (mean-motion) resonant angles $2\lambda_c - \lambda_c - \varpi_b$ and $2\lambda_c - \lambda_c - \varpi_c$. It is interesting that despite this chaotic behavior, the effective lifetimes of these orbits are relatively long. We expect longer integrations would reveal

¹⁶ We use ϖ to refer to the planet's orbit as opposed to ω_* , which refers to the star's orbit.

unstable behavior.

In conclusion, this limited look into the long-term stability of the orbital solutions to the RV data suggests that orbits with large eccentricities are plausible, even if the system fails the Hill criterion, if the system is in resonance.

4.4. Sub-Saturn Planets

Here, we put the EPIC-203771098 system in the context of the other sub-Saturns. Figure 6 shows the densities and radii of planets having $R_P = 4\text{--}8 R_\oplus$ and density measured to better than 50%, i.e. $\sigma(\rho)/\rho < 50\%$. The symbol colors represent the planet equilibrium temperature assuming zero albedo, and the symbol shapes indicate whether TTVs or RVs were used to measure planet mass. The EPIC-203771098 planets are labeled in bold. The EPIC-203771098 planets are fairly typical compared other sub-Saturn planets.

The relative sizes and densities of the EPIC-203771098bc pair are reminiscent of the Kepler-18cd pair. Kepler-18c has a mass of $17.3 \pm 1.9 M_\oplus$, radius of $5.49 \pm 0.26 R_\oplus$, and a density of 0.59 g cm^{-3} , similar to EPIC-203771098b. Kepler-18d has a mass of $16.4 \pm 1.4 M_\oplus$, a radius of $6.98 \pm 0.33 R_\oplus$, and a density of $0.27 \pm 0.03 \text{ g cm}^{-3}$. While Kepler-18b is smaller and less massive than EPIC-203771098c, it has a similar density. Kepler-18cd also lie near the 2:1 mean-motion resonance (Cochran et al. 2011).

While there are still relatively few sub-Saturns with well-measured masses and radii, there are some trends worth noting. Densities measured from TTVs tend to be lower than RV-measured densities. This trend was noted by Weiss & Marcy (2014) for planets smaller than $4 R_\oplus$. Here, we offer some observational and astrophysical explanations. The Doppler semi-amplitude, K , depends primarily on planet mass, and has a weaker dependence on orbital period, eccentricity, and stellar mass. The TTV technique is also sensitive to planet mass; that sensitivity is amplified by a system's proximity to resonance. See Steffen (2015) for a more complete comparison of the sensitivities associated with TTVs and RVs. Thus, it is perhaps not surprising that the lowest density (i.e., lowest mass) sub-Saturns have more TTV than RV measurements. Lee & Chiang (2015a) offer a parallel astrophysical explanation: TTV measurements are most easily made for systems in or near mean-motion resonances; such resonant systems formed by convergent inward migration; the planets comprising a resonant system therefore formed at larger orbital distances where disk gas was colder, less dense, and optically thinner; such gas cools more rapidly and is therefore accreted more readily onto rocky cores, forming especially low-density ("super-puffy") planets (see also Section 4.2).

4.5. Follow-up Opportunities

4.5.1. TTVs

Due to the proximity of EPIC-203771098b & c to the 2:1 mean-motion resonance, coherent gravitational interactions between the planets will result in large TTVs. Lithwick et al. (2012) developed an analytic theory to describe TTVs near first order resonances, i.e. $j+1:j$ resonances where j is an integer. We use this theory to estimate, within an order of magnitude, the amplitude

of TTVs in this system. Following Lithwick et al. (2012), the normalized distance to resonance is given by

$$\Delta \equiv \frac{P'}{P} \frac{j-1}{j} - 1,$$

where P is the period of the inner planet and P' is the period of the outer planet. For the EPIC-203771098bc pair, $j = 2$ and $\Delta = 0.014$. Near resonance, TTVs are oscillatory with a "super period" given by

$$P^j = \frac{P'}{j\Delta}.$$

For the EPIC-203771098bc pair, P^j is 1490 d or ≈ 4 years.

Another important quantity that influences TTVs is Z_{free} , a linear combination of the free complex eccentricities of the two planets.¹⁷ When $|Z_{\text{free}}| \ll |\Delta|$ or $|Z_{\text{free}}| \gg |\Delta|$ the amplitude of the TTV signal, $|V|$, is given by equations 14 and 15 in Lithwick et al. (2012):

$$|V| \sim P \frac{\mu'}{|\Delta|} \left(1 + \frac{|Z_{\text{free}}|}{|\Delta|} \right) \quad (1)$$

and

$$|V'| \sim P' \frac{\mu}{|\Delta|} \left(1 + \frac{|Z_{\text{free}}|}{|\Delta|} \right), \quad (2)$$

where $\mu = M_P/M_\star$. We consider a useful limiting case where $|Z_{\text{free}}| \ll |\Delta|$. In this case, the respective TTV amplitudes of planets b and c are

$$|V| \sim P \frac{\mu'}{|\Delta|} \sim 2.6 \text{ hr} \quad (3)$$

and

$$|V'| \sim P' \frac{\mu}{|\Delta|} \sim 4.0 \text{ hr.} \quad (4)$$

Given that EPIC-203771098 is bright ($V = 11.3$) and that the planets are large, TTVs of this magnitude are easily detectable from the ground. We emphasize that the TTVs can be significantly larger when $|Z_{\text{free}}| \approx e > |\Delta| \approx 0.01$, and so the nominal TTV amplitude estimated above provides a rough lower limit to the TTV amplitude. Strictly speaking, however, there are some "coincidental" orbital configurations with $|Z_{\text{free}}| \sim \Delta$ where the TTV amplitudes could be smaller than the above estimates. However, such configurations are rare (see Lithwick et al. 2012). Given that $|Z_{\text{free}}|$ depends on e_b , e_c , ϖ_b , and ϖ_c , observing and modeling the TTVs over an appreciable fraction of the 4 yr super period will place important constraints on the orbits of EPIC-203771098b and c.

4.5.2. Transmission Spectroscopy

The fact that EPIC-203771098b and c are large, low-density, and orbit a bright host star ($V = 11.3$) makes

¹⁷ For a more detailed discussion of Z_{free} and how it relates to the forced and free eccentricities of both planets, see Lithwick et al. (2012)

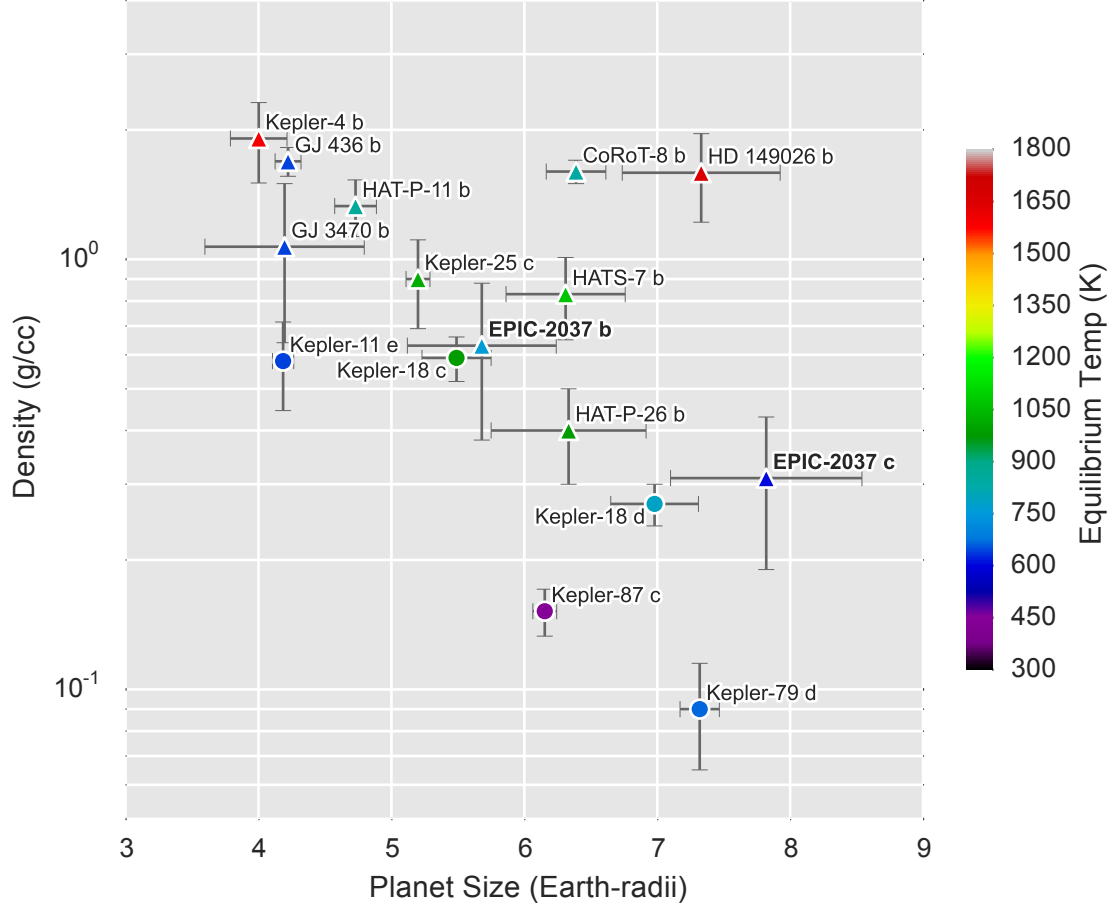


FIG. 6.— Planet radii and densities for planets having $R_P = 4\text{--}8 R_\oplus$ where density is measured to better than 50%. The symbol color represents the (zero-albedo) equilibrium temperature. The symbol shape indicates the observational technique used to measure planet mass. Triangles and circles represent RV and TTV measurements, respectively. Planets taken from the Exoplanet Orbit Database and from Bakos et al. (2015).

them especially favorable targets for atmospheric characterization via transmission spectroscopy. Such observations could directly test our conclusions about the planets' bulk composition and formation history by measuring their atmospheres' elemental compositions and overall metal enrichments. For cloud-free, hydrogen-dominated atmospheres, we expect features in the transmission spectra to have amplitudes of $\sim 10H R_P/R_\star^2$, where H is the atmospheric scale height (Miller-Ricci et al. 2009), which corresponds to ~ 250 ppm and ~ 400 ppm for planets b and c, respectively.

Features of this size should be detectable even with current instrumentation on the *Hubble Space Telescope*. We note that, given the high-altitude clouds or hazes frequently seen in exoplanet atmospheres, the spectral features of the EPIC-203771098 planets could be wholly muted at *HST*-accessible wavelengths. However, in just a few years, high-precision spectroscopy with *JWST* should be capable of detecting the strongest absorption features (e.g. by CO_2 at 4–5 μm ; Morley et al. 2015). By measuring the thermal emission spectra, MIRI should handily detect the planets' expected 10 μm eclipse depths of ~ 100 ppm (Greene et al. 2015, in press). Future observations will measure the atmospheric makeup of these and other low-density sub-Saturns and so begin to elucidate

the nature of these mysterious objects.

5. CONCLUSIONS

We have presented the discovery and characterization of two sub-Saturn-sized planets orbiting EPIC-203771098 detected by *K2* in Campaign 2. We conducted follow-up adaptive optics imaging and spectroscopy of EPIC-203771098 and found that it is a single, metal-rich ($[\text{Fe}/\text{H}] = 0.42 \pm 0.04$ dex) G3 star. We confirmed the two planets using Keck/HIRES by measuring the changes in the radial velocity of EPIC-203771098 due to its planets. Our RV measurements also constrain planet mass, density, and interior structure. EPIC-203771098b has a size of $5.68 \pm 0.56 R_\oplus$ and a mass of $21.0 \pm 5.4 M_\oplus$. EPIC-203771098c is larger and more massive, having $R_P = 5.68 \pm 0.56 R_\oplus$ and $M_P = 27.0 \pm 6.9 M_\oplus$.

We combined the measured sizes and masses of EPIC-203771098b and c with the interior structure models of Lopez & Fortney (2013), to constrain the likely distribution of planet mass between core and envelope. According to these models, $\sim 75\%$ of EPIC-203771098b's mass ($17.6 \pm 4.3 M_\oplus$) is concentrated in its core. EPIC-203771098c has a similar core mass, $16.1 \pm 4.2 M_\oplus$, but that only comprises $\sim 50\%$ of its total mass. We explored the possible formation scenarios of EPIC-203771098b & c and hypothesize that the planets formed exterior to

their current locations, and migrated inward as a resonant pair. We have difficulty explaining how EPIC-203771098c nearly doubled in mass without undergoing runaway accretion to form a Jovian-mass planet. We encourage further follow-up of these planets using TTVs to constrain the orbits and dynamical state of the system and with transmission spectroscopy to measure atmospheric composition and structure. We also encourage further study of planets in the sub-Saturn size range. While the current sample of sub-Saturns around bright stars is quite small, upcoming *K2* Campaigns along with future missions like *TESS* and *PLATO* should reveal many more.

We thank Geoffrey Marcy, Konstantin Batygin, and Leslie Rogers for helpful discussions. E. A. P. acknowledges support from a Hubble Fellowship grant HST-HF2-51365.001-A awarded by the Space Telescope Science Institute, which is operated by the Association of Universities for Research in Astronomy, Inc. for NASA under contract NAS 5-26555. A. W. H. acknowledges support for our *K2* team through a NASA Astrophysics Data Analysis Program grant. A. W. H. and I. J. M. C. acknowledge support from the *K2* Guest Observer Program. E. D. L. received funding from the European Union Seventh Framework Programme (FP7/2007-2013) under grant agreement number 313014 (ETAEARTH). B. J. F. acknowledges support from a National Science

Foundation Graduate Research Fellowship under grant No. 2014184874. Any opinion, findings, and conclusions or recommendations expressed in this material are those of the authors and do not necessarily reflect the views of the National Science Foundation. This research used resources of the National Energy Research Scientific Computing Center, a DOE Office of Science User Facility supported by the Office of Science of the U.S. Department of Energy under Contract No. DE-AC02-05CH11231. This work made use of the SIMBAD database (operated at CDS, Strasbourg, France), NASA's Astrophysics Data System Bibliographic Services, and data products from the Two Micron All Sky Survey (2MASS), the APASS database, the SDSS-III project, and the Digitized Sky Survey. Some of the data presented in this paper were obtained from the Mikulski Archive for Space Telescopes (MAST). Support for MAST for non-HST data is provided by the NASA Office of Space Science via grant NNX09AF08G and by other grants and contracts. Some of the data presented herein were obtained at the W. M. Keck Observatory (which is operated as a scientific partnership among Caltech, UC, and NASA). The authors wish to recognize and acknowledge the very significant cultural role and reverence that the summit of Maunakea has always had within the indigenous Hawaiian community. We are most fortunate to have the opportunity to conduct observations from this mountain.

Facility: *Kepler*, *K2*, Keck-I (HIRES), Keck-II (NIRIC2)

REFERENCES

Albrecht, S., Winn, J. N., Johnson, J. A., et al. 2012, *ApJ*, 757, 18
 Bakos, G. Á., Penev, K., Bayliss, D., et al. 2015, *ApJ*, 813, 111
 Barnes, R., & Greenberg, R. 2007, *ApJ*, 665, L67
 Byrd, R. H., P. Lu, P., & J., N. 1995, *SIAM Journal on Scientific and Statistical Computing*, 16, 1190
 Cochran, W. D., Fabrycky, D. C., Torres, G., et al. 2011, *ApJS*, 197, 7
 Coelho, P., Barbuy, B., Meléndez, J., Schiavon, R. P., & Castilho, B. V. 2005, *A&A*, 443, 735
 Crossfield, I. J. M., Petigura, E., Schlieder, J. E., et al. 2015, *ApJ*, 804, 10
 Cumming, A., Butler, R. P., Marcy, G. W., et al. 2008, *PASP*, 120, 531
 Deck, K. M., & Batygin, K. 2015, *ApJ*, 810, 119
 Delfosse, X., Forveille, T., Mayor, M., et al. 1998, *A&A*, 338, L67
 Dotter, A., Chaboyer, B., Jevremović, D., et al. 2008, *ApJS*, 178, 89
 Eastman, J., Gaudi, B. S., & Agol, E. 2013, *PASP*, 125, 83
 Foreman-Mackey, D., Hogg, D. W., Lang, D., & Goodman, J. 2013a, *PASP*, 125, 306
 —. 2013b, *PASP*, 125, 306
 Fressin, F., Torres, G., Charbonneau, D., et al. 2013, *ApJ*, 766, 81
 Gladman, B. 1993, *Icarus*, 106, 247
 Han, E., Wang, S. X., Wright, J. T., et al. 2014, *PASP*, 126, 827
 Howard, A. W., Johnson, J. A., Marcy, G. W., et al. 2010, *ApJ*, 721, 1467
 Howard, A. W., Marcy, G. W., Bryson, S. T., et al. 2012, *ApJS*, 201, 15
 Howard, A. W., Marcy, G. W., Fischer, D. A., et al. 2014, *ApJ*, 794, 51
 Howell, S. B., Sobeck, C., Haas, M., et al. 2014, *PASP*, 126, 398
 Huber, D., Chaplin, W. J., Christensen-Dalsgaard, J., et al. 2013, *ApJ*, 767, 127
 Inamdar, N. K., & Schlichting, H. E. 2015, *MNRAS*, 448, 1751
 Isaacson, H., & Fischer, D. 2010, *ApJ*, 725, 875
 Jones, E., Oliphant, T., Peterson, P., et al. 2001, *SciPy: Open source scientific tools for Python*, [Online; accessed 2015-10-21]
 Kolbl, R., Marcy, G. W., Isaacson, H., & Howard, A. W. 2015, *AJ*, 149, 18
 Kreidberg, L. 2015, ArXiv e-prints, arXiv:1507.08285
 Lee, E. J., & Chiang, E. 2015a, ArXiv e-prints, arXiv:1510.08855
 —. 2015b, *ApJ*, 811, 41
 Lee, E. J., Chiang, E., & Ormel, C. W. 2014, *ApJ*, 797, 95
 Liddle, A. R. 2004, *MNRAS*, 351, L49
 Lithwick, Y., Xie, J., & Wu, Y. 2012, *ApJ*, 761, 122
 Liu, S.-F., Hori, Y., Lin, D. N. C., & Asphaug, E. 2015, *ApJ*, 812, 164
 Lopez, E. D., & Fortney, J. J. 2013, *ApJ*, 776, 2
 —. 2014, *ApJ*, 792, 1
 Lucy, L. B., & Sweeney, M. A. 1971, *AJ*, 76, 544
 Marchal, C., & Bozis, G. 1982, *Celestial Mechanics*, 26, 311
 Marcy, G. W., & Butler, R. P. 1992, *PASP*, 104, 270
 Marcy, G. W., Butler, R. P., Fischer, D., et al. 2001, *ApJ*, 556, 296
 Marcy, G. W., Butler, R. P., Vogt, S. S., Fischer, D., & Lissauer, J. J. 1998, *ApJ*, 505, L147
 Milani, A., & Nobili, A. M. 1983, *Celestial Mechanics*, 31, 213
 Miller-Ricci, E., Seager, S., & Sasselov, D. 2009, *ApJ*, 690, 1056
 Morley, C. V., Fortney, J. J., Marley, M. S., et al. 2015, ArXiv e-prints, arXiv:1511.01492
 Morton, T. D. 2015, *isochrones: Stellar model grid package*, Astrophysics Source Code Library, ascl:1503.010
 Murray, C. D., & Dermott, S. F. 2000, *Solar System Dynamics*
 Parviainen, H., & Aigrain, S. 2015, *MNRAS*, 453, 3821
 Petigura, E. A. 2015, PhD thesis, University of California, Berkeley
 Petigura, E. A., Howard, A. W., & Marcy, G. W. 2013, *Proceedings of the National Academy of Science*, 110, 19273
 Petigura, E. A., Schlieder, J. E., Crossfield, I. J. M., et al. 2015, *ApJ*, 811, 102
 Pollack, J. B., Hubickyj, O., Bodenheimer, P., et al. 1996, *Icarus*, 124, 62
 Rivera, E. J., Laughlin, G., Butler, R. P., et al. 2010, *ApJ*, 719, 890
 Schwarz, G. 1978, *Annals of Statistics*, 6, 461
 Steffen, J. H. 2015, ArXiv e-prints, arXiv:1510.04750
 Torres, G., Fischer, D. A., Sozzetti, A., et al. 2012, *ApJ*, 757, 161

Valenti, J. A., Butler, R. P., & Marcy, G. W. 1995, PASP, 107, 966

Valenti, J. A., & Fischer, D. A. 2005, ApJS, 159, 141

Vogt, S. S., Allen, S. L., Bigelow, B. C., et al. 1994, 2198, 362

Weiss, L. M., & Marcy, G. W. 2014, ApJ, 783, L6

Winn, J. N., Johnson, J. A., Howard, A. W., et al. 2010, ApJ, 718, 575

Wisdom, J., & Holman, M. 1991, AJ, 102, 1528

Wisdom, J., Holman, M., & Touma, J. 1996, Fields Institute Communications, Vol. 10, p. 217, 10, 217

Zacharias, N., Finch, C. T., Girard, T. M., et al. 2012, VizieR Online Data Catalog, 1322, 0